Shear instability and gravity wave saturation in an asymmetrically stratified jet

W.D. Smyth* and J.N. Moum
College of Oceanic and Atmospheric Sciences
Oregon State University, Corvallis OR 97331-5503

Submitted July 17th, 2001.

* Corresponding author. Telephone: (541) 737-3029; email: smyth@coas.oregonstate.edu

Abstract

Motivated by the mean current and stratification structure associated with the Equatorial Undercurrent (EUC), we examine the stability and wave propagation characteristics of a highly idealized model flow: the asymmetrically stratified jet. This is a parallel shear flow in which the depth-varying current has the sech^2 form of a Bickley jet. The stratification has a step function structure: the buoyancy frequency takes uniform values above and below the center of the jet, with the larger value occurring below. The spectrum contains three classes of unstable normal modes. Two are extensions of the sinuous and varicose modes of the unstratified Bickley jet; the third has not been described previously. The asymmetric stratification structure allows instabilities to radiate gravity wave energy from the upper flank of the jet to the lower flank, where it encounters a critical layer. From here, wave energy may be reflected, absorbed or transmitted. Absorption results in wave saturation and momentum transfer to the mean flow, in close analogy with the breaking of orographic gravity waves in the middle atmosphere. Transmission beyond the lower flank may partly account for wave signals observed in the deep equatorial ocean. All of these processes exert zonal forces on the jet that alter its speed and shape. The wave structures and associated fluxes developed by the idealized model are compared with observations of the EUC.

Keywords:
instability, internal waves, jets, stratified shear flow.

1 Introduction

A dominant component of the tropical ocean current system is the equatorial undercurrent (EUC), a region of intense turbulence associated with shear instability and internal gravity wave radiation. Our purpose here is to explore some of the fundamental properties of instability and wave radiation in this regime via stability analysis and numerical simulation of a simple model flow.

The EUC flows eastward at a depth of approximately 100m, spans a meridional range of a few hundred km centered on the equator, and has a maximum speed near 1m/s. The current is a nearly permanent feature in both Atlantic and Pacific oceans, and is forced by the zonal pressure

gradient that builds up due to westward transport of surface water by the Trade Winds (e.g. Veronis (1960), see Qiao and Weisberg (1997) for a recent discussion). Interannual fluctuations in the strength of the Pacific EUC are an integral component of the El Nino - Southern Oscillation (ENSO) cycle.

Shear on the upper and lower flanks of the EUC drives much of the strong turbulence that characterizes the equatorial oceans (Moum et al., 1989; Peters et al., 1989). The resulting vertical momentum flux distributes momentum input from the wind into the upper ocean and thereby provides a partial counterbalance to the zonal pressure gradient (Hebert et al., 1991). The EUC is also a region of strong internal gravity wave (IGW) activity, which may also account for significant momentum fluxes (Moum et al., 1989; Lien et al., 1996). Dillon et al. (1989) found that momentum fluxes due to turbulence act over a relatively shallow layer adjacent to the surface (i.e. much shallower than the layer over which the zonal pressure gradient acts), and therefore suggested that fluxes due to IGW are also needed to explain the observed current structure.

Application of normal mode stability analysis to the EUC began with Sutherland (1996), who demonstrated that the upper flank of the EUC may support shear instabilities that act to radiate energy downward in the form of IGW. Mack and Hebert (1997) and Sun et al. (1998) showed that the dominant IGW signal observed in the equatorial Pacific is associated with this class of instabilities. Using observed profiles of velocity and density, Sun et al. (1998) demonstrated that shear instability can flux momentum to the deepest reaches of the EUC, in accordance with the suggestion of Dillon et al. (1989) discussed above. In order that these results be applicable under a range of equatorial flow regimes, the mechanisms of instability must be understood more thoroughly. To this end, we are analyzing a sequence of simple models that converge towards an accurate representation of the EUC and whose instability mechanisms are both broadly relevant and accessible to detailed study (as opposed to the highly complex and flow-specific instabilities of measured currents, e.g. Sun et al. (1998)). Our hypothesis is that the EUC exists, on average, in a nearly stable state, but that this state is frequently perturbed by fluctuations in forcing. The flow adjusts to these perturbations via a range of instability mechanisms that lead to property fluxes via waves and turbulence. We begin here with a model that isolates the dominant features of the shear and stratification that characterize the EUC.

The stability characteristics of the EUC are governed in large part by a distribution of stable density stratification that is asymmetric with respect to the current. In particular, stratification tends to be weak on the upper flank of the current, which includes the wind-driven South Equatorial Current and the surface mixed layer (figure 1a,b). Because of this asymmetry, typical values of the gradient Richardson number tend to be smaller on the upper flank (often close to or less than the critical value 1/4) and larger on the lower flank (figure 1c).

Unstable modes of a jetlike current such as the EUC each possess a pair of critical levels (levels at which the mean flow velocity matches the phase velocity of the mode), one on each flank of the jet. A wave energy flux incident on a critical level interacts with the mean flow, with the result that it is divided into reflected, absorbed, and transmitted components. The details of this division depend largely on the local value of the gradient Richardson number, Ri. If $Ri < 1/4$ at the critical level, the wave may be over-reflected, i.e. it may gain energy from the mean flow during the interaction, so that the sum of the reflected and transmitted components is greater than the incoming flux. This process is thought to be a central aspect of shear instability (e.g. Lindzen and Tung, 1978; Smyth and Peltier, 1989). If $Ri > 1/4$ at the critical level, over-reflection cannot occur, and waves lose energy to the mean flow. In this case, trapping of wave energy near the

critical layer leads to turbulent breakdown via convective instability (Winters and D'Asaro, 1993; Lin et al., 1993; Winters and D'Asaro, 1994).

The asymmetric distribution of stratification in the EUC raises the possibility of modes that have local Richardson number less than 1/4 at the upper critical level but greater than 1/4 at the lower critical level. In such a case, we expect that wave energy will be radiated from the upper critical level downward through the jet core and to the lower critical level. Some of this energy will then be reflected back to the upper critical level, sustaining the instability. Some of the energy may be transmitted through the lower critical level, possibly propagating to great depths. Finally, some energy may be absorbed at the lower critical level, causing momentum transfer and turbulent mixing. The pattern of turbulence observed in the EUC is suggestive of the processes described above, with enhanced turbulence occurring on the lower flank of the jet where the Richardson number is relatively high (figure 1d, $z < -160m$). This mechanism is analogous to the saturation of orographic gravity waves in the middle atmosphere. Parameterization of the momentum flux divergences generated by that wave-mean flow interaction has turned out to be crucial to the accuracy of atmospheric general circulation models (e.g. Lindzen, 1981; Fritts, 1989).

Here, we investigate instability and wave radiation in the EUC using the simplest possible model, the asymmetrically stratified jet (figure 2). The undercurrent is represented by a sech^2 velocity profile, i.e. a Bickley jet (Drazin and Reid, 1981). The buoyancy frequency is described by a step function whose value changes at the center of the jet (see section 2 for details). This model is relevant to any jetlike current that exists far from boundaries in the presence of asymmetric stratification, atmospheric jet streams being another example. To correspond with the EUC, we let the larger value of the buoyancy frequency occur in the lower half-space, but the properties of

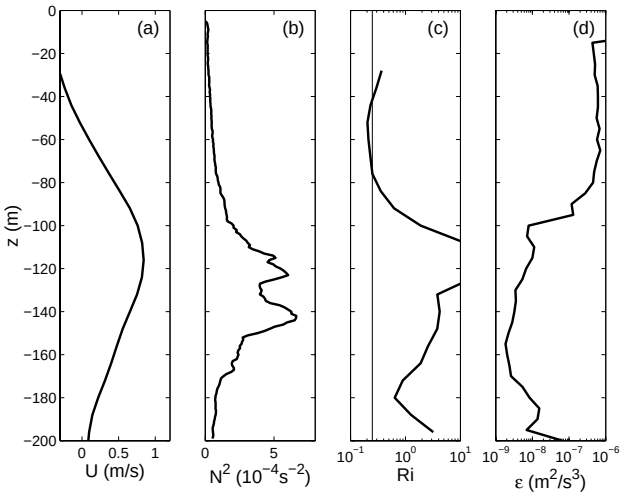

Figure 1: Observations taken aboard the R/V Wecoma at 0^oN, 140^oW, during the Tropical Instability Wave Experiment (Lien et al., 1995). Profiles are averaged over year days 311-315, inclusive, of 1991. (a) Zonal velocity, (b) squared buoyancy frequency, (c) gradient Richardson number (the vertical line marks the critical value 1/4), (d) kinetic energy dissipation rate.

a jet with stratification larger above its core are obtained trivially from the present results.

Instabilities of the stratified Bickley jet were first studied numerically by Hazel (1972). This work was continued by Sutherland and Peltier (1992) and Sutherland et al. (1994), who added a region of uniform flow to the center of the jet. Here, we extend these investigations by allowing the stratification to be asymmetric with respect to the current. Sutherland (1996) studied waves and instability specific to the EUC using a model that included the boundary at the surface, but which represented the mean current as a hyperbolic tangent shear layer, thus isolating the upper flank the EUC. He allowed stratification to be weaker above the shear layer than below, and showed that this promotes the growth of unstable modes that couple efficiently with the deeper IGW spectrum. The Bickley jet employed in the present study provides a more realistic representation of the EUC than the shear layer, and allows

us to extend the results of Sutherland by looking explicitly at the reflection, absorption and transmission of energy at the lower critical level. In future publications, we will extend this model to include effects of the surface boundary and the SEC, as well as the seasonal thermocline. Here, we focus on the effects of asymmetric stratification in isolation from such complications. We approach the stability of the asymmetrically stratified jet as a problem of general relevance, as well as focussing on those aspects most germane to the EUC.

Background flow profiles used in the analyses are described in section 2. Section 3 contains the main results of the investigation. Linear stability analyses are used to establish the spectrum of normal mode instabilities at various values of stratification parameters. In section 4, the results are tested in the nonlinear regime by means of two-dimensional numerical simulations. The results are compared with observations of gravity waves the EUC in section 5. Section 6 contains a summary and concluding discussion.

2 Background states

Our mathematical model employs the Boussinesq equations in a physical space measured by the Cartesian coordinates $\{x_*, y_*, z_*\}$. For most analyses, flow will be restricted to the x_* and z_* directions. Asterisks are used to indicate dimensional quantities; all other quantities are nondimensionalized using velocity scale u_o and the length scale h_o.

The nondimensional velocity field $U(x, y, z, t)$ is given at $t = 0$ by the standard Bickley jet:

$$U(x, y, z, 0) = \text{sech}^2 z. \tag{1}$$

A nondimensional buoyancy, $\theta(x, z, t)$, is defined in terms of the density $\rho(x, z, t)$, its representative value ρ_o and the gravitational acceleration g_* as

$$\theta = -\frac{\rho - \rho_o}{\rho_o} \times \frac{g_* h_o}{u_o^2}. \tag{2}$$

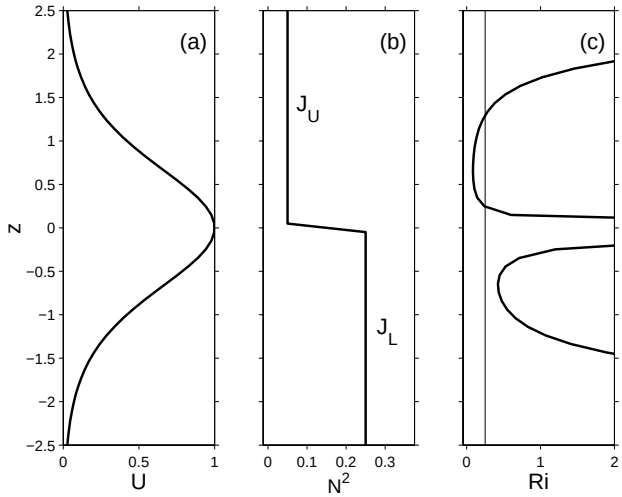

Figure 2: Background profiles defining the asymmetrically stratified jet. (a) Velocity; (b) Buoyancy gradient; (c) gradient Richardson number. For this case, $J_L = 0.25$ and $J_U = 0.05$.

In a fluid where density is controlled only by temperature, θ is proportional to the temperature deviation. The initial nondimensional buoyancy field is defined (up to an arbitrary additive constant) by

$$N^2 \equiv \frac{\partial}{\partial z}\theta(x, y, z, 0) = \begin{cases} J_U, & z > 0 \\ J_L, & z \le 0. \end{cases} \tag{3}$$

The constants J_U and J_L are bulk Richardson numbers that characterize upper and lower layer stratification in comparison with the shear associated with the jet.

3 Linear stability analyses of normal modes

3.1 Methods

The stability analyses are based on the usual Taylor-Goldstein equation for linear normal modes of an inviscid,

stratified, parallel, Boussinesq shear flow:

$$\frac{d^2\hat{\psi}}{dz^2} + \gamma^2(z)\hat{\psi} = 0; \tag{4}$$

$$\gamma^2(z) = \frac{N^2}{(U-c)^2} - \frac{d^2U/dz^2}{U-c} - \alpha^2. \tag{5}$$

The streamfunction has been assumed to have the normal mode form:

$$\psi(x,z,t) = \Psi(z) + \mu\hat{\psi}(z)\exp[i\alpha(x-ct)] \tag{6}$$

in which μ is an ordering parameter and α and c are the nondimensional streamwise wavenumber and phase velocity. Only the real parts of the perturbations are physically relevant. We assume that the modes of primary interest are two-dimensional (i.e. the wavevector is parallel to the background flow), but oblique modes are obtained easily via Squire's transformation (Drazin and Reid, 1981) and will be discussed where relevant. $U(z) = -d\Psi/dz$ and $N^2 = d\Theta/dz$ are the background profiles of velocity and buoyancy gradient (squared buoyancy frequency) as given by (1) and (3).

To minimize boundary effects, we impose the radiation condition $d\hat{\psi}/dz = i\gamma\hat{\psi}$ at both upper and lower boundaries, with the sign of γ chosen in each case to eliminate incoming waves (Hazel, 1972; Sun et al., 1998). The resulting eigenvalue problem is solved numerically using the multiple shooting method of Hazel (1972). Because linear theory does not specify absolute mode amplitudes, we normalize the eigenfunctions so that

$$\max_z \hat{\psi} = 1. \tag{7}$$

Eigenfunctions for perturbation quantities other than the streamfunction are recovered using the polarization relations:

$$\begin{aligned} \hat{w} &= i\alpha\hat{\psi} \\ \hat{u} &= -\hat{\psi}_z \\ \hat{\pi} &= (\bar{u}-c)\hat{\psi}_z - \bar{u}_z\hat{\psi} \\ \hat{\omega} &= -(\alpha^2+\gamma^2)\hat{\psi} \\ \hat{\theta} &= \frac{-N^2}{U-c}\hat{\psi} \end{aligned} \tag{8}$$

For each set of background profiles (i.e. for each set of values for J_L and J_U), we scan over α to identify classes of unstable modes. We then choose representative members of each class for more detailed study. The typical choice is the mode for which the exponential growth rate, given by $\sigma = \alpha c_i$ where c_i is the imaginary part of the phase speed, is a maximum.

Energetics of the linear, inviscid model are described by the perturbation kinetic energy equation:

$$\frac{\partial K}{\partial t} = -\frac{\partial\bar{u}}{\partial z}\cdot\overline{u'w'} + \overline{w'\theta'} - \frac{\partial}{\partial z}\overline{\pi'w'}. \tag{9}$$

The overbar indicates a horizontal average and primes denote fluctuations about that average. $K = \frac{1}{2}(\overline{u'^2} + \overline{w'^2})$ is the perturbation kinetic energy and π is a scaled pressure. The remaining quadratic quantities, $\overline{u'w'}$, $\overline{w'\theta'}$ and $\overline{\pi'w'}$ correspond to vertical fluxes of horizontal momentum, buoyancy and kinetic energy. To compute the flux profiles, the real parts of the relevant eigenfunctions are multiplied, then averaged over one wavelength in x using the standard relation $\overline{a'b'} = \frac{1}{2}\text{Real}(\hat{a}^*\hat{b})$.

A useful quantity for the characterization of energy partitioning is the flux Richardson number, defined here as

$$R_f = -\frac{\int\overline{w'\theta'}dz}{\int\overline{u'w'}dz}. \tag{10}$$

The momentum flux $\overline{u'w'}$ is of additional interest because, at second order in μ, it affects the mean flow via the evolution equation

$$\frac{\partial\bar{u}}{\partial t} = -\frac{\partial}{\partial z}\overline{u'w'}. \tag{11}$$

This effect is of central importance in the application of our results to the EUC.

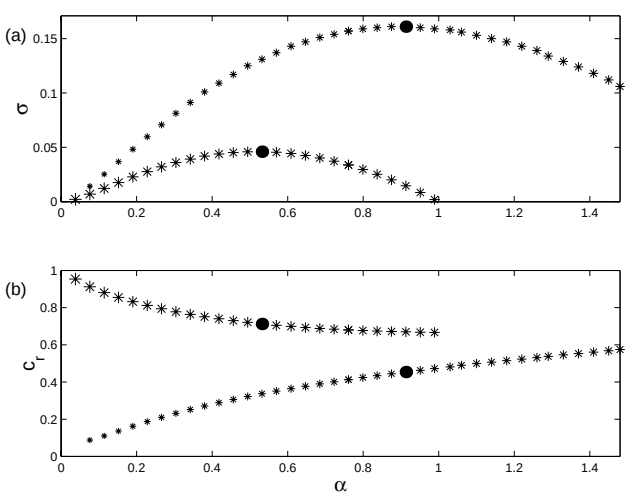

Figure 3: Nondimensional growth rate (a) and phase speed (b) as a function of nondimensional wavenumber for unstable modes of the classical Bickley jet ($J_L = J_U = 0$). Symbol size varies linearly with phase speed to aid in identification. Bullets indicate the fast growing mode in each class.

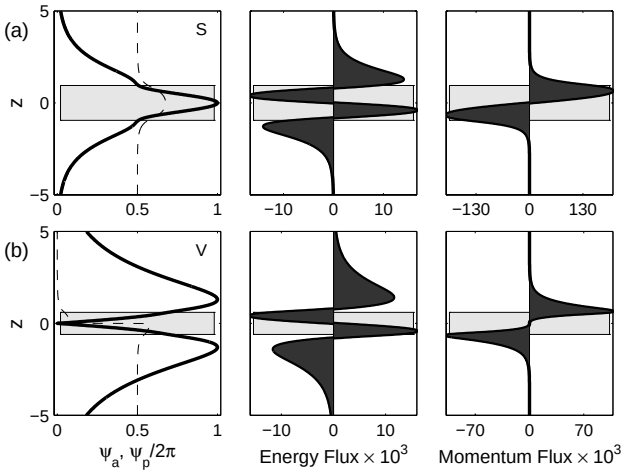

Figure 4: Eigenmodes of the most unstable sinuous (a) and varicose (b) modes for the unstratified Bickley jet ($J_L = J_U = 0$). Leftmost column gives the magnitude of the eigenfunction $\hat{\phi}(z)$ (solid curve), normalized by its maximum value, as well as the phase normalized by 2π (dashed curve). Remaining columns show vertical fluxes of energy $\overline{p'w'}$ and momentum $\overline{u'w'}$, respectively. Shaded boxes indicate the region between the upper and lower critical levels.

3.2 Results

As a point of departure, we briefly review the sinuous and varicose instabilities of the Bickley jet with $J_L = J_U = 0$ (Drazin and Reid, 1981). Figure 3 shows spectra of the growth rate and phase speed, indicating the existence of the two classes of unstable modes whose properties vary continuously as a function of wavenumber. Each class exhibits a well-defined wavenumber at which the growth rate is a maximum (bullets on figure 3). The sinuous mode dominates at all wavenumbers, and attains its maximum growth rate near $\alpha = 1$ (figure 3a). The varicose mode is most unstable at twice the wavelength, and exhibits higher phase speeds than the sinuous mode. Figure 4 shows the eigenfunctions of the fastest-growing members of each mode class. The streamfunction of the sinuous mode (figure 4a) is even with respect to $z = 0$, whereas the varicose mode is odd, i.e. undergoes a phase shift at $z = 0$. Each mode extracts energy from the mean flow near both the upper and lower critical levels, as is evident from the energy flux profiles in figure 4. Each mode is configured so as to flux momentum outward away from the jet core, thus tending to broaden and weaken the jet.

We now begin our discussion of stratification effects with a survey of the growth rate of the fastest growing mode at each point on the (J_L, J_U) plane (figure 5). The special case $J_U = J_L$ was investigated by Hazel (1972) and, as a limiting case, by Sutherland and Peltier (1992). As $J_U = J_L$ increases, the growth rate drops monotonically and vanishes near $J_U = J_L = 0.13$. The nature of the dependence of the growth rate on stratification changes when either J_L or J_U (but not both) exceeds a critical value, which ranges between 0.17 and 0.22 (thin curves on figure 5). In this regime, the growth rate becomes nearly independent of the larger of the two strati-

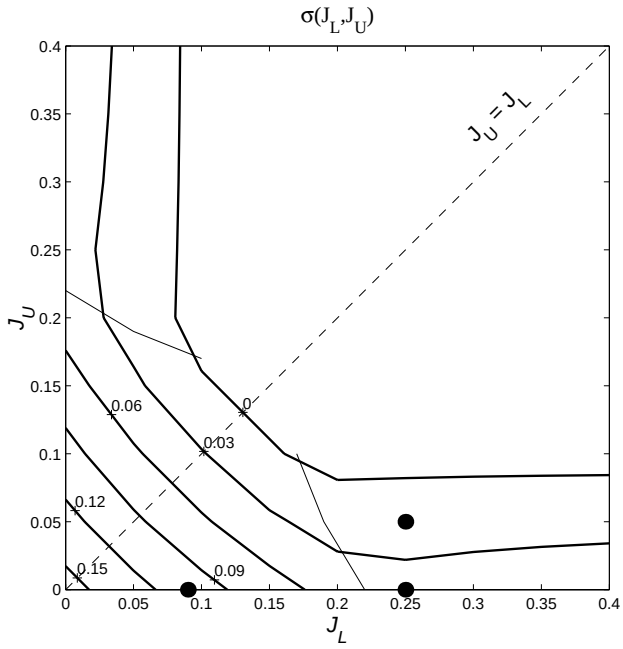

Figure 5: Growth rate of the most unstable mode as a function of J_L and J_U. Thin curves indicate the boundaries beyond which instability becomes approximately independent of the larger of J_L and J_U. Bullets indicate points at which more detailed analyses are described later in this section.

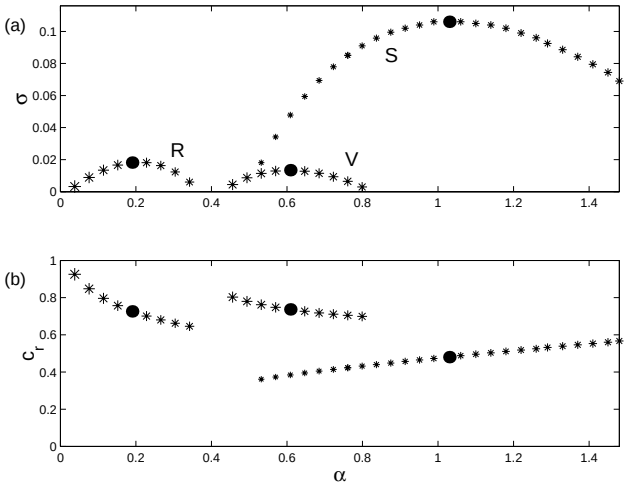

Figure 6: Nondimensional growth rate (a) and phase speed (b) as a function of nondimensional wavenumber for unstable modes of the asymmetrically stratified jet with $J_L = 0.09$ and $J_U = 0$. Labels indicate the mode classes. Symbol size varies linearly with phase speed.

fication parameters. Instability persists at arbitrarily large values of the stratification in either the upper or the lower half-space, as long as the stratification in the other half space is sufficiently weak. It is this asymmetric stratification regime that is of primary interest to us in this paper. We will demonstrate that instability in this regime is driven by a previously undiscovered mechanism.

We first examine the effect of adding weak stratification to the lower half-space by setting J_L equal to 0.09. The analysis now reveals three distinct classes of unstable modes (figure 6). Eigenfunctions for the fastest-growing member of each class are shown in figure 7. Two of the mode classes are extensions of the sinuous and varicose modes of the unstratified case, and we will refer to them as the S and V modes, respectively. The presence of stratification acts to damp the S mode slightly and the V mode more strongly (figure 6). In addition, growth rate maxima for both modes are shifted to higher wavenumbers. Both modes disappear at low wavenumbers and are replaced by a new mode class, denoted "R". The existence of this new mode is the main result of the present investigation, and its characteristics will be described presently.

The reason for the preferential stabilization of the V mode is evident upon inspection of the energy flux profiles in figures 7a and b (second column). Not surprisingly, both the S and V modes have lost their symmetry about $z = 0$. The S mode now extracts energy from the mean flow preferentially at the upper critical level, while the V mode extracts energy mainly at the lower critical level. The V mode is thus affected more strongly by the stable stratification in the lower half-space. This distinction is also evident in the buoyancy flux profiles (fourth column), which indicate that the V mode does more work against

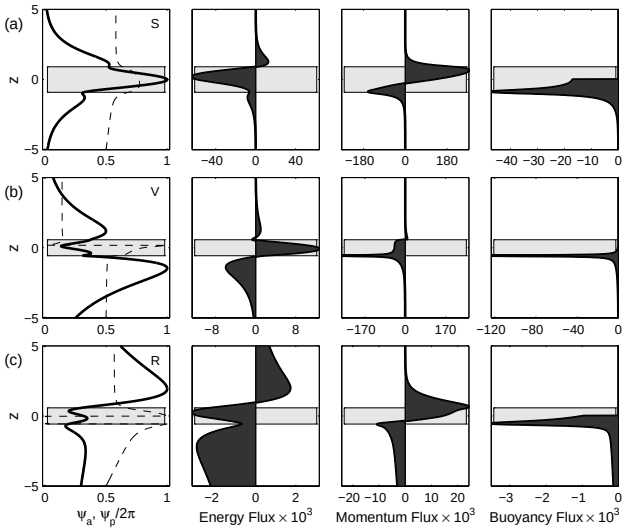

Figure 7: Eigenmodes of the most unstable S (a), V (b) and R (c) modes for the asymmetrically stratified jet with $J_L = 0.09$ and $J_U = 0$. Leftmost column gives the magnitude of the eigenfunction $\hat{\psi}(z)$ (solid curve), normalized by its maximum value, as well as the phase normalized by 2π (dashed curve). Remaining columns show vertical fluxes of energy $\overline{p'w'}$, momentum $\overline{u'w'}$ and buoyancy $\overline{\theta'w'}$, respectively. Shaded boxes indicate the region between the upper and lower critical levels.

gravity, relative to its amplitude, than does the S mode. In every case, the buoyancy flux is strongly focussed at the lower critical level. The flux Richardson numbers of the V and S modes are 0.44 and 0.16, respectively. Note that the momentum flux due to the V mode (figure 7b, third column) is nearly flat except near the critical levels. This is a general characteristic of weak instabilities (Eliassen and Palm, 1961).

The asymmetry of the momentum flux has an interesting implication for the motion of the jet as a whole. The centroid of the velocity distribution is

$$\zeta = \frac{\int z\bar{u}dz}{\int \bar{u}dz}, \tag{12}$$

where the integrals cover the (possibly infinite) vertical extent of the flow. Differentiating ζ with respect to time, substituting (11), and assuming that the flux vanishes at the boundaries, we obtain

$$\frac{d\zeta}{dt} = \frac{\int \overline{u'w'}dz}{\int \bar{u}dz}. \tag{13}$$

The integral of the momentum flux thus indicates the direction in which the centroid moves as the mode grows to finite amplitude. The flux due to the S mode tends to raise the centroid of the jet. This finite-amplitude effect moves the shear away from the stratified region, the overall effect of which is to lower the Richardson number and enhance the growth of the instability. In contrast, the V mode acts to move the jet downward into the stratified region.

The new mode class seen in figure 6 resembles the S mode in that it extracts energy from the mean flow primarily near its upper critical level (figure 7c). As a result, it does relatively little work against gravity. The new mode differs most dramatically from both the S and V modes in the region below the lower critical level: it drives strong fluxes of energy, momentum and buoyancy downward into the lower half plane. The tilt in the phase profile of the eigenfunction indicates a uniform phase progression with depth, indicative of wavelike signal propagation. In other words, the phase speed and wavelength of this mode are such that it excites an IGW field in the lower half plane having a real vertical wavenumber. For this reason, we refer to the new instability as the R (for "radiating") mode.

Note that the amplitude of the R mode is not uniform in the region below the jet; rather, it decays exponentially with depth. This behavior should not be confused with evanescence, the decay of signals that do not resonate with any propagating mode. The decay seen here is due to the fact that the source of the radiation is a disturbance that grows exponentially with time. The wave amplitude also grows exponentially with time at any fixed depth. At a fixed time, however, the signal is strongest at points nearest to the source. Exponential growth is also responsible for the nonzero buoyancy flux carried into the lower half

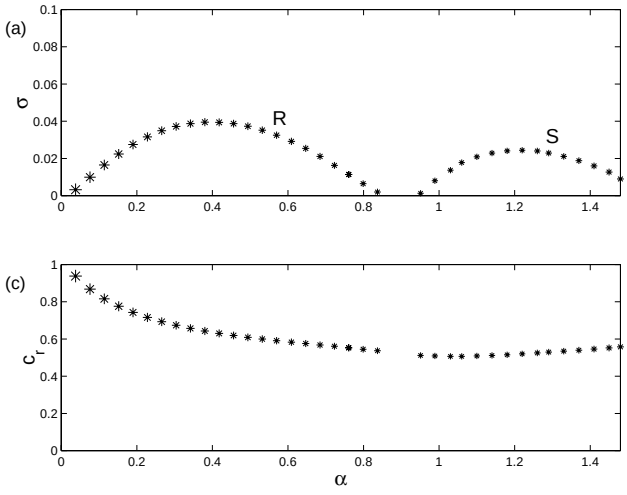

Figure 8: Nondimensional growth rate (a) and phase speed (b) as a function of nondimensional wavenumber for unstable modes of the asymmetrically stratified jet with $J_L = 0.25$ and $J_U = 0$. Labels indicate the mode classes. Symbol size varies linearly with phase speed.

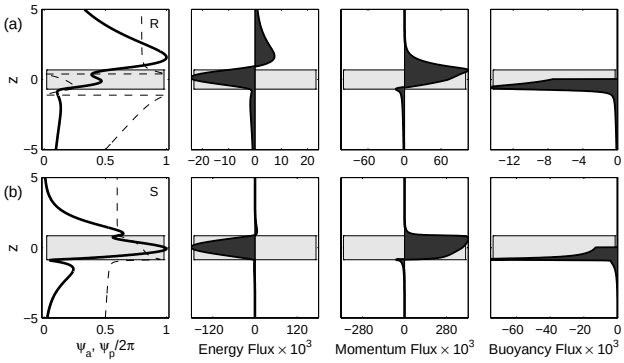

Figure 9: Eigenmodes of the most unstable R (a) and S (b) modes for the asymmetrically stratified jet with $J_L = 0.25$ and $J_U = 0$. Leftmost column gives the magnitude of the eigenfunction $\hat{\psi}(z)$, normalized by its maximum value, as well as the phase normalized by 2π. Remaining columns show vertical fluxes of energy $\overline{p'w'}$, momentum $\overline{u'w'}$ and buoyancy $\overline{\theta'w'}$, respectively. Shaded boxes indicate the region between the upper and lower critical levels.

plane by the R mode.

Next, we examine the effect of stronger stratification in the lower half-space, the case $J_L = 0.25$. The V mode is now entirely stabilized, and the growth rate of the fastest-growing R mode is faster than that of the fastest-growing S mode (figure 8). Turning to the energy flux profiles (figure 9, second column), we see that the R mode still radiates energy into the lower half plane as in the previous case, but that energy flux is much weaker than before (relative to the amplitude of the perturbation streamfunction, cf. figure 7c). Although the wavelength and phase speed allow the R mode to resonate with a free IGW mode, very little of the mode's energy is able to penetrate beyond the lower critical level. The S mode also fluxes very little energy into the lower half-space and, as before, it does not resonate with any vertically propagating mode. For both modes, the buoyancy flux is focussed near the lower critical level. The flux Richardson number of the S mode has increased to 0.28, indicating that the mode expends a significant fraction of the energy it gains from the mean flow in doing work against gravity.

The modes shown in figure 9 clearly illustrate our hypothesized mechanism in which gravity waves are launched by instability on the upper flank of the jet, propagate downward through the jet core, and are absorbed at the lower critical level. Note in particular the intense divergence of the momentum flux just above the lower critical level of the S mode (figure 9b, third column). At finite amplitude, this divergence will lead to a rapid deceleration of the mean flow and consequent upward migration of the critical level in analogy with orographic waves in the atmosphere (Fritts, 1989). This mechanism may account for turbulence observed on the lower flank of the EUC (figure 1d) and may play an important role in the zonal momentum balance.

Having looked closely at the specific cases $J_L = 0$, $J_L = 0.09$ and $J_L = 0.25$, we now take a broader

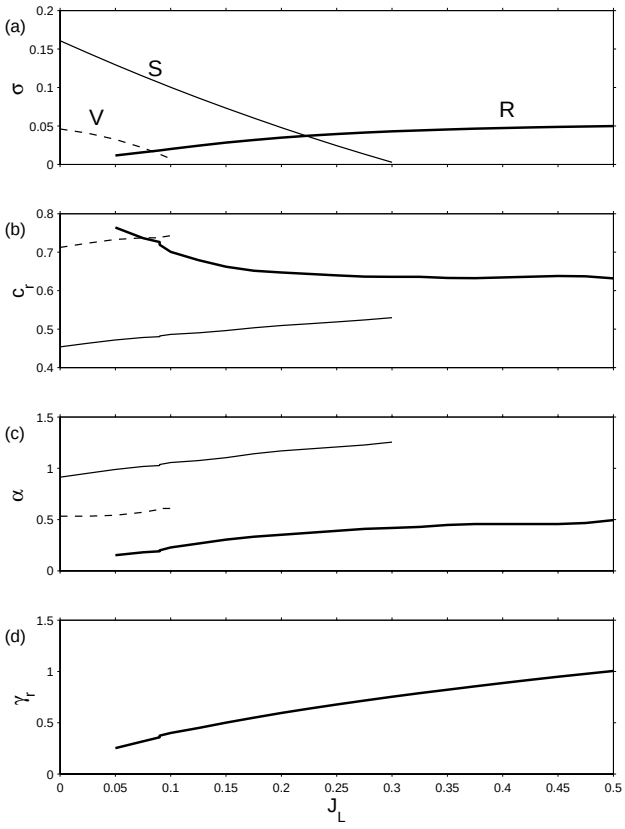

Figure 10: Scalar properties of the fastest growing modes as functions of stratification parameter J_L for the case $J_U = 0$. Thin, thick and dashed curves indicate the fastest-growing S, R and V modes, respectively. (a) Growth rate. (b) Phase speed. (c) Streamwise wavenumber. (d) Real vertical wavenumber of the corresponding free mode, given by (5).

view of the dependence of the stability characteristics of the asymmetrically stratified jet upon the lower stratification parameter J_L . Figures 10, 11 and 12 show various scalar properties of the S, V and R mode classes as functions of J_L with $J_U = 0$. For each class, the mode illustrated is that which maximizes the growth rate. The S and V modes are both stabilized by the stratification: the former is damped entirely for $J_L > 0.3$, while the latter is damped for $J_L > 0.1$. The R mode appears to be destabilized as soon as J_L is increased above zero (though it is difficult to detect numerically at very small J_L). The R mode becomes the dominant instability for $J_L > 0.22$. The growth rate continues to increase with increasing stratification, up to and beyond the largest J_L value shown here. The reasons for this relative freedom from buoyancy damping will be explored below.

Both the R and V modes have much larger phase speeds than the S mode, indicating that their critical layers are located close to the jet core, while the critical layers of the S mode lie further out on the flanks of the jet (figure 10b).

For all modes, the dominant wavenumber increases slightly with increasing stratification. The R mode is the longest, exceeding the S mode in wavelength by a factor of three or more at all J_L (figure 10c). This difference accounts for the R mode's ability to couple efficiently with freely propagating gravity waves in the lower half-space. In fact, the R mode is the only mode that couples to a free mode with real vertical wavenumber (figure 10d). The vertical wavenumber at which the R mode radiates increases strongly with increasing stratification. Over the range shown in figure 10, the vertical wavenumber is about twice the horizontal wavenumber.

The local Richardson number at the lower critical level, Ri_L, varies approximately in proportion to J_L, and is nearly the same for all three modes. Because the V mode grows by extracting energy from the mean flow at the lower critical level, we expect that it will be damped for all $Ri_L > 1/4$. In fact, Ri_L=0.18 at the largest J_L for which the V mode is unstable. For larger J_L, only the two modes that extract energy at the upper critical level are unstable.

In general, instability in strongly stratified cases requires that modes be configured so as to expend only a small fraction of their energy uptake in doing work against gravity. Because its energy source is in the stratified region, the V mode expends a large fraction of its energy

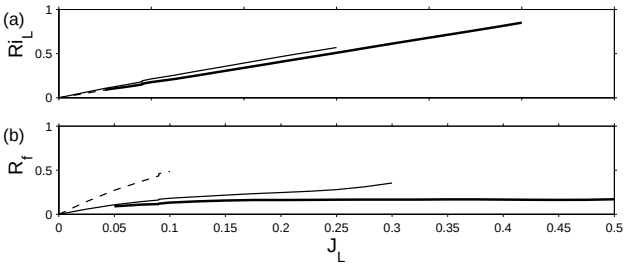

Figure 11: Scalar properties of the fastest growing modes as functions of J_L for the case $J_U = 0$. Thick, thin and dashed curves indicate the fastest-growing S, R and V modes, respectively. (a) Gradient Richardson number at the lower critical level. (b) Flux Richardson number.

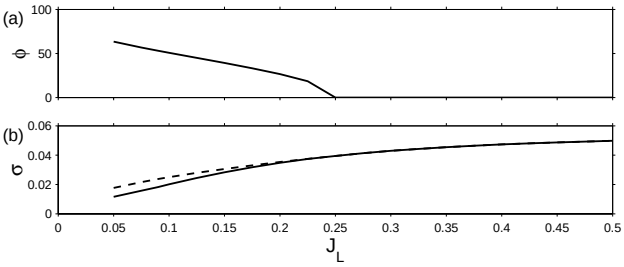

Figure 12: Scalar properties of the fastest growing R mode as functions of J_L for the case $J_U = 0$. (a) Angle between the wavevector and the x axis. (b) Growth rates of the fastest growing mode (dashed) and the fastest growing two-dimensional mode (solid).

working against gravity. By the time the mode disappears at $J_L = 0.1$, its flux Richardson number is about 0.5 (figure 11b). The flux Richardson number of the S mode increases more slowly, reaching a value 0.38 at the largest J_L for which the instability exists. In contrast, the R mode is configured so as to do relatively little work against gravity even at the largest J_L values included here, and is therefore able to grow despite strong stratification in the lower half plane.

The fact that the R mode is destabilized by stratification raises the possibility that the fastest growing mode may be oblique, i.e. it may have a nonzero spanwise component to its wavevector. In unstratified flow, Squire's theorem (Drazin and Reid, 1981) shows that, while they always exist, no oblique mode can be the fastest growing. In the presence of stratification, however, Squire's theorem is modified so that the growth rate of a three-dimensional mode is related to that of a two-dimensional mode at higher bulk Richardson number (e.g. Smyth and Peltier, 1990). Any mode class whose growth rate increases with increasing stratification has the potential to have an oblique mode as its fastest growing member. As long as the mean flow is parallel, the growth rate is always even with respect to the spanwise component of the wavevector. Oblique modes are therefore expected to occur in pairs, having equal growth rates and phase speeds but directed at opposite angles from the streamwise direction. Smyth et al. (1988) noted that the fastest growing mode is oblique in any region of parameter space where the growth rate increases faster than $J^{1/2}$ (where J is a bulk Richardson number).

In the present case, the growth rate of the R mode increases faster than $J_L^{1/2}$ for all J_L less than 0.25. Figure 12a shows the angle by which the wave vector of the fastest growing mode departs from the x axis. This angle is large for small J_L, but decreases to zero by $J_L = 0.25$. The R mode is therefore two-dimensional over most of the large J_L values for which it is the fastest growing instability. An exception to this occurs in the small range $0.22 < J_L < 0.25$, where a three-dimensional R mode dominates. However, the difference in growth rate between this and the corresponding two-dimensional mode is less than one half percent (figure 12b). In the nonlinear simulations described in the next section, we will examine two-dimensional modes only.

We complete the description of the linear normal modes of the asymmetrically stratified jet by returning briefly to the case in which the upper level stratification parame-

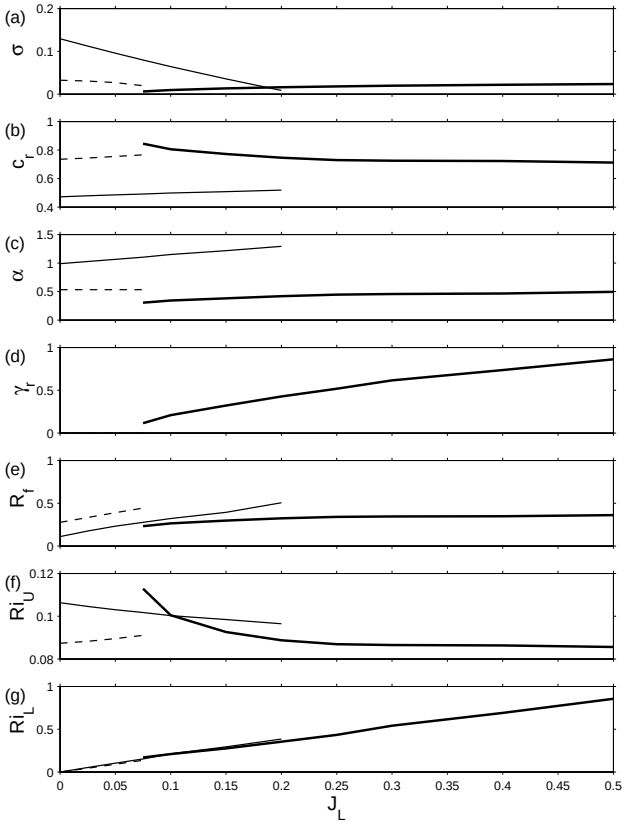

Figure 13: Scalar properties of the fastest growing modes as functions of J_L for the case $J_U = 0.05$. Thick, thin and dashed curves indicate the fastest-growing S, R and V modes, respectively. (a) Growth rate. (b) Phase speed. (c) Streamwise wavenumber. (d) Real vertical wavenumber of the corresponding free mode. (e) Flux Richardson number. Gradient Richardson number at the upper (f) and lower (g) critical level.

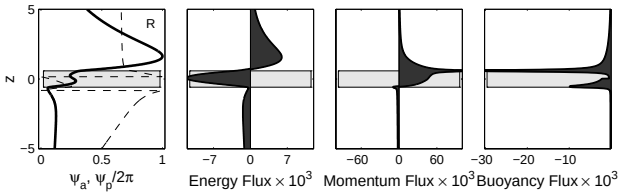

Figure 14: Eigenmodes of the most unstable R mode for the asymmetrically stratified jet with $J_L = 0.25$ and $J_U = 0.05$. Leftmost frame gives the magnitude of the eigenfunction $\hat{\psi}(z)$, normalized by its maximum value, as well as the phase normalized by 2π. Remaining frames show vertical fluxes of energy $\overline{p'w'}$, momentum $\overline{u'w'}$ and buoyancy $\overline{\theta'w'}$, respectively. Shaded boxes indicate the region between the upper and lower critical levels.

ter J_U is nonzero. Scalar parameters for $J_U = 0.05$ are shown as functions of J_L in figure 13. Comparing with the case $J_U = 0$ (figures 10 and 11), we see that the growth rates are reduced by the upper level stratification. The S and V modes are damped at lower values of J_L , and the asymptotic growth rate of the R mode at large J_L is reduced by about one half. The phase speeds of all modes are increased somewhat (figure 13b), indicating that their critical levels have moved toward the jet core. The streamwise wavenumbers at which the modes are most unstable are not significantly changed from the $J_U = 0$ case (figure 13c), but the vertical wavenumber at which the R mode resonates is reduced (figure 13d). Because the stratification is now nonzero at the upper critical level, the two modes (S and R) that extract their energy from the mean flow in that region do more work against gravity, with the result that their flux Richardson numbers are generally higher (figure 13e). The gradient Richardson number at the upper critical level is now nonzero in all cases, but it remains substantially smaller than 1/4 for each unstable mode (figure 13f). The gradient Richardson number at the lower critical level (figure 13g) is slightly reduced, but it retains the property of being essentially equal for the fastest growing mode of each class. The R mode at $J_L = 0.25$, $J_U = 0.05$ now shows a significant buoyancy flux at the upper critical level, but its tendency to radiate energy into the lower half-space is unchanged from the $J_U = 0$ case (figure 14, cf. figure 9a).

4 Nonlinear simulations

The unstable normal modes described in the previous section have the potential to grow to large amplitude, and thus to generate large fluxes of energy and momentum and a vigorous turbulent energy cascade. Since linear theory tells us nothing about the amplitude a given instability will attain, it does not allow us to evaluate the strength of these processes in any real geophysical system. To estimate the actual fluxes and mixing rates requires solution of the fully nonlinear initial value problem. To do this in detail, particularly for a flow of geophysical scale, is beyond the scope of the present study. However, a strongly constrained nonlinear model offers the opportunity to make useful first estimates.

Because the dominant linear instabilities of parallel shear flows tend to be two-dimensional, it makes sense to investigate their evolution to large amplitude via simulations in which motions in the third dimension are suppressed. In these simulations, the effects of small-scale turbulence are represented only crudely via a diffusion operator. Aspects of the flow for which these motions are crucial, such as turbulent mixing at critical levels, cannot be evaluated with any confidence. However, these simulations are expected to deliver realistic amplitudes for the large-scale aspects of the flow evolution, in particular the fluxes due to wave propagation.

4.1 Methods

To take full advantage of the restriction to two dimensions, the nondimensional Boussinesq equations are cast in vorticity-streamfunction form as:

$$\frac{\partial \omega}{\partial t} = \frac{\partial \psi}{\partial z}\frac{\partial \omega}{\partial x} - \frac{\partial \psi}{\partial x}\frac{\partial \omega}{\partial z} + \frac{\partial \theta}{\partial x} + \frac{1}{Re}\nabla^2(\omega - \bar{\omega}) \tag{14}$$

$$\frac{\partial \theta}{\partial t} = \frac{\partial \psi}{\partial z}\frac{\partial \theta}{\partial x} - \frac{\partial \psi}{\partial x}\frac{\partial \theta}{\partial z} + \frac{1}{RePr}\nabla^2(\theta - \bar{\theta}) + D_\theta(x,z,t) \tag{15}$$

$$\omega = \nabla^2 \psi \tag{16}$$

The fields $\omega(x,z,t)$ and $\psi(x,z,t)$ represent vorticity and the streamfunction, respectively, while $\theta(x,z,t)$ represents the buoyancy as before. The Reynolds number $Re = u_o h_o/\nu$ represents the reciprocal of the nondimensional kinematic viscosity. Pr denotes the Prandtl number, the ratio of viscosity to scalar diffusivity. For the present experiments, we choose $Re = 300$ and $Pr = 1$. Note that the diffusion operators are not applied to the horizontally-averaged flow (denoted by overbars). D_θ represents a radiative damping term to be described below.

The numerical model approximates solutions to the initial value problem defined by (14-16), together with periodic boundary conditions in x and flux-free boundary conditions at the upper and lower limits of the computational domain. Spatial discretization is Fourier pseudospectral in the horizontal, second-order centered difference in the vertical. Temporal discretization is via a second-order Adams-Bashforth method.

In order to mimic the radiation boundary conditions employed in the linear analyses (section 3.1), the computational domain is divided into an inner "physical" layer and outer sponge layers. In the sponge layers, Rayleigh damping is applied to the scalar field so as to minimize the reflection of gravity waves back into the physical layer. The damping coefficient increases smoothly from zero at the edge of the physical layer, reaching a maximum value of $\gamma = 0.20$ at the boundary of the computational domain, e.g.:

$$D_\theta = -\gamma \frac{1}{2}\big(1 - \cos \pi \frac{z_b - z}{z_b - z_B}\big)(\theta - \bar{\theta}) \tag{17}$$

where z_b and z_B denote the lower boundaries of the physical and computational domains, respectively. Within the

physical domain, $D_\theta = 0$. The vertical grid spacing is uniform within the physical domain, but varies in the sponge layers. The grid interval increases linearly from its physical-domain value at the inner edge of the sponge layer to three times that value at the domain boundary. Flow diagnostics are computed over the physical domain only.

Initial conditions consist of basic states as defined in section 2, with added perturbations proportional to the unstable normal modes computed in section 3. The perturbation amplitudes are chosen so that the perturbation kinetic energy is 10^{-4} times the kinetic energy of the mean flow at $t = 0$. The physical domain is defined by $0 \le x < L$; $-5 \le z \le 5$, where L is some integer multiple of the wavelength of the eigenfunction. Upper and lower sponge layers extend to $z = 9$ and $z = -13$.

We have used this methodology to investigate the nonlinear evolution of many of the unstable modes described in the previous section. Here, we describe three particular cases that encompass the range of nonlinear behaviors found. In each case, the initial condition consists of a mean flow specified by the values of J_L and J_U, plus a small perturbation proportional to the eigenfunction of some linear normal mode. In the first case, the mean flow is characterized by $J_L = 0.14$, $J_U = 0$, so that stratification in the lower half-space is significant but the S mode still dominates. This run is designated S14. The second case, denoted R25, has $J_L = 0.25$, $J_U = 0$, so that the R mode dominates. For the third simulation, we retain $J_L = 0.25$ but increase J_U to 0.05, to see the effect of stratification in the upper half space. This run is denoted R2505.

4.2 Results

The evolution of the perturbation kinetic energy, spatially averaged over the physical domain, is shown for our three cases in figure 15. Not surprisingly, the modes with the largest linear growth rates exhibit the most rapid initial increase in kinetic energy. For case S14, K grows to a maximum near t=50, then decays slowly. The radiating mode with $J_L = 0.25$ and $J_U = 0$ (R25) grows more slowly at first, but exhibits a sharp increase in growth rate after about t=60 and eventually attains larger energy than the S case. The reason for this late growth phase will be explored below. The R mode with $J_L = 0.25$ and $J_U = 0.05$ (R2505) grows slowly throughout the simulation.

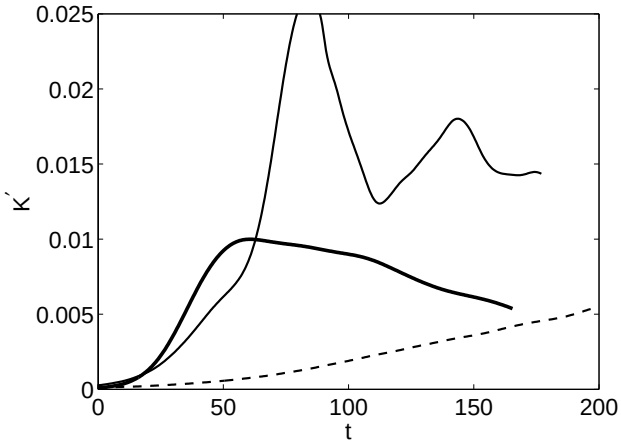

Figure 15: Volume-averaged perturbation kinetic energy as a function of time for simulations S14 (thick solid), R25 (thin solid) and R2505 (dashed).

The temperature, vorticity and perturbation streamfunction fields for the S mode at t=40 and t=80 are shown in figure 16. Three wavelengths of the primary instability are included in the computational domain to facilitate subsequent comparison with the longer R modes. The counterclockwise (positive) vorticity of the upper flank of the jet is concentrated into discrete monopoles, while the lower flank vorticity appears as curved braids (figure 16, middle frames). The maximum clockwise vorticity (thick contours) is larger than the maximum counterclockwise vorticity (thin contours), due to the baroclinic torque exerted by the buoyancy force. The upper edge of the stratified fluid is distorted into smooth ripples (figure 16, left

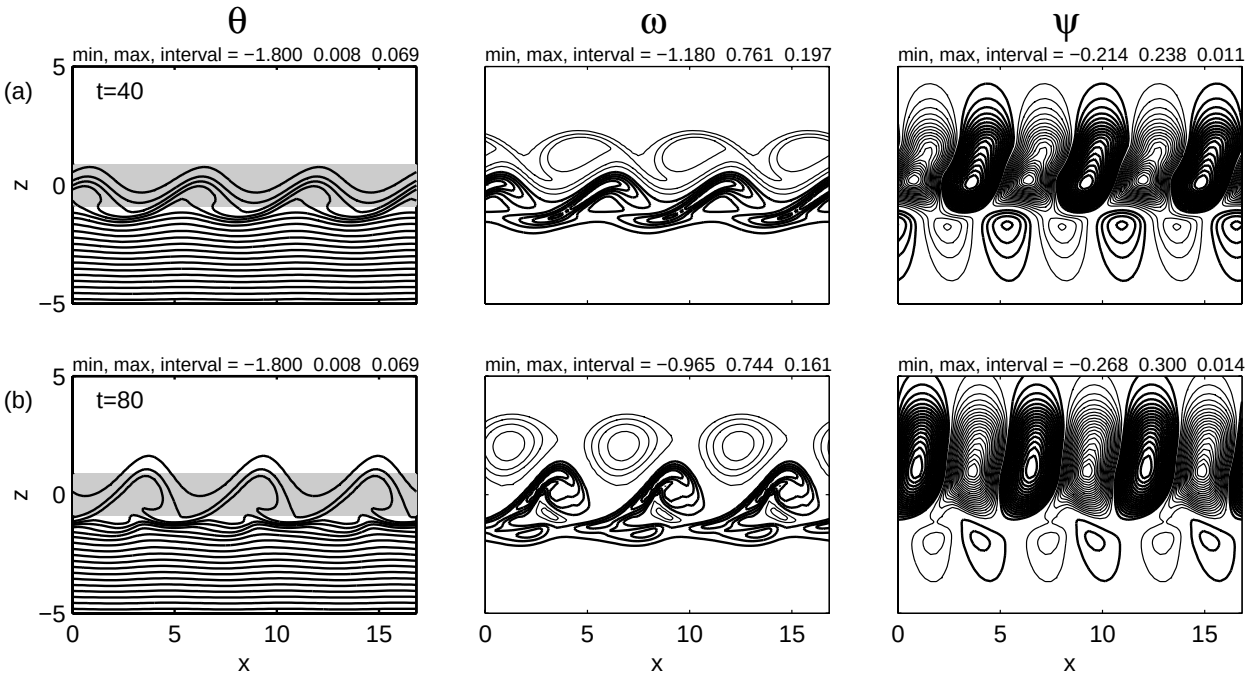

Figure 16: Scaled temperature, vorticity and perturbation streamfunction fields for run S14 at t=40 (a) and t=80 (b). The perturbation streamfunction is defined relative to the horizontally-averaged profile. Shading indicates the original locations of the critical levels. For the vorticity and the streamfunction, thick (thin) contours indicate negative (positive) values.

hand frames). Further down, however, the scalar field exhibits large amplitude overturns. This enhanced displacement begins at the lower critical level, and indicates intense wave-mean flow interaction in that region (figure 16a, left frames, bottom of shaded region). Enhanced turbulence observed on the lower flank of the EUC (figure 1d) may result from a similar mechanism. By t=80, (figure 16b), the overturning region has migrated upward due to wave-induced acceleration of the mean flow.

Beyond this point in the flow evolution, it is likely that a fully three-dimensional simulation would reveal motions in the spanwise direction. Secondary stability analyses of shear-driven billows (e.g. Klaassen and Peltier, 1985b; Sutherland et al., 1994) have revealed that three-dimensional motions become important once K reaches its maximum value. Analyses of waves approaching a critical level by Winters and D'Asaro (1994) have shown a similar result: overturns break down partly via three-dimensional convective motions. Ultimately, our two-dimensional flow approaches a state of nonlinear equilibrium, with continued slow evolution due only to diffusion.

The R mode (figure 17) is distinguished from the S mode by its large wavelength (cf. figure 10c) and slow growth (figure 10a, figure 15). At $t = 40$, flow distortions due to the R mode are relatively weak. The perturbation streamfunction exhibits wave radiation into the lower half plane, as expected on the basis of the stability analyses. By $t = 60$, the disturbance has reached large amplitude and exhibits strong vorticity and distinct overturning near the lower critical level. The long wave is now modulated

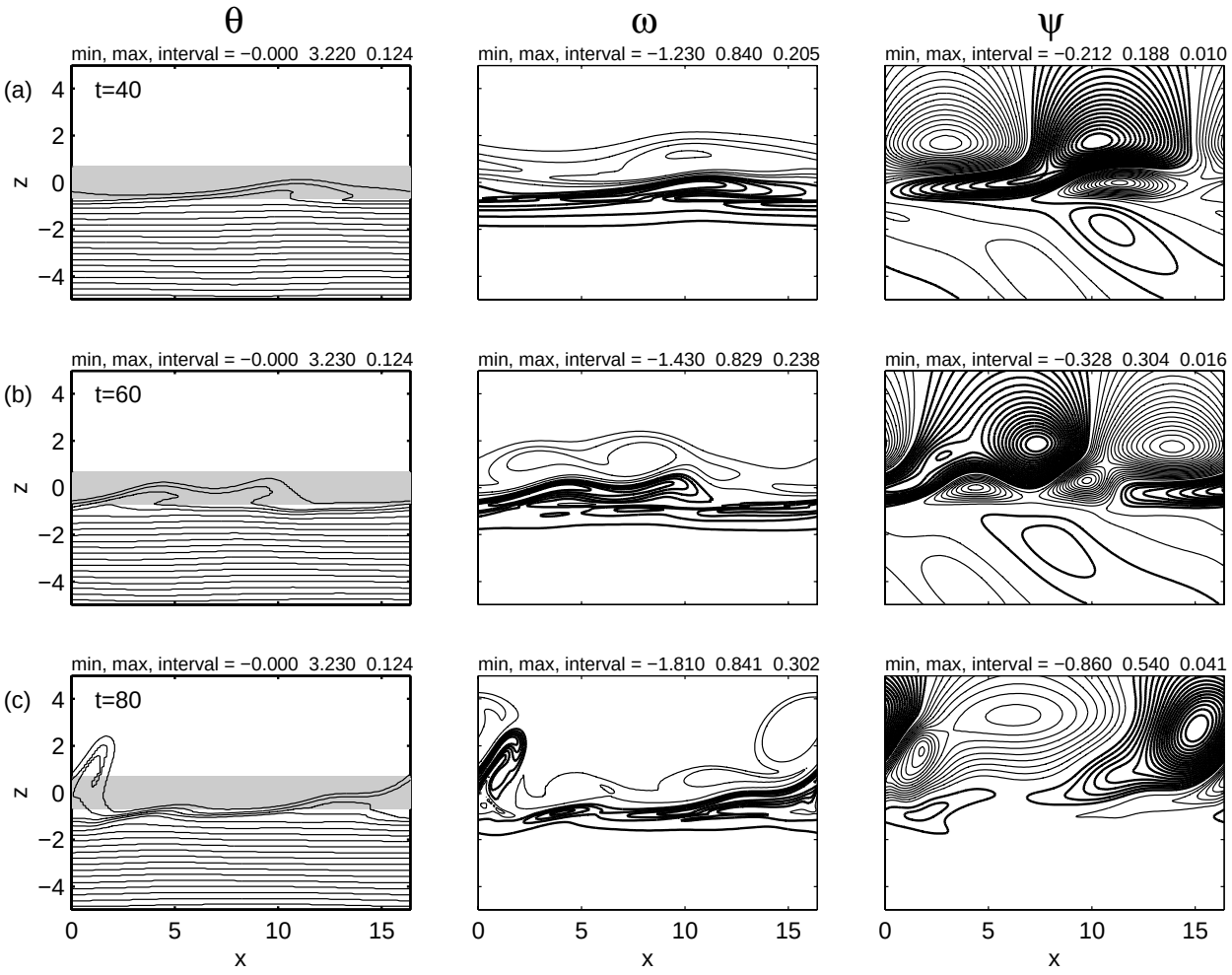

Figure 17: Scaled temperature, vorticity and perturbation streamfunction fields for run R25 at t=40 (a), t=60 (b) and t=80 (c). The perturbation streamfunction is defined relative to the horizontally- averaged profile. Shading indicates the original locations of the critical levels. For the vorticity and the streamfunction, thick (thin) contours indicate negative (positive) values.

by a disturbulence of shorter wavelength.

By $t = 80$, the character of the disturbance that originated with the R mode has changed dramatically. The flow is now dominated by a large amplitude, short wavelength disturbance. Strong overturning is evident. The short-wave disturbance has caused long plumes of stratified fluid to be ejected into the upper half plane. Not long after this, the jet is completely disrupted by the large amplitude disturbance. (By this point, the flow is certain to be influenced by three-dimensional effects, so the present results must be treated as preliminary. It seems unlikely, however, that three-dimensional motions would alter the main features of the flow.) Downgoing radiation in the lower half-space is still present at $t = 80$, though it is weak in comparison with the intense vortices above the jet and is therefore not visible in figure 17c.

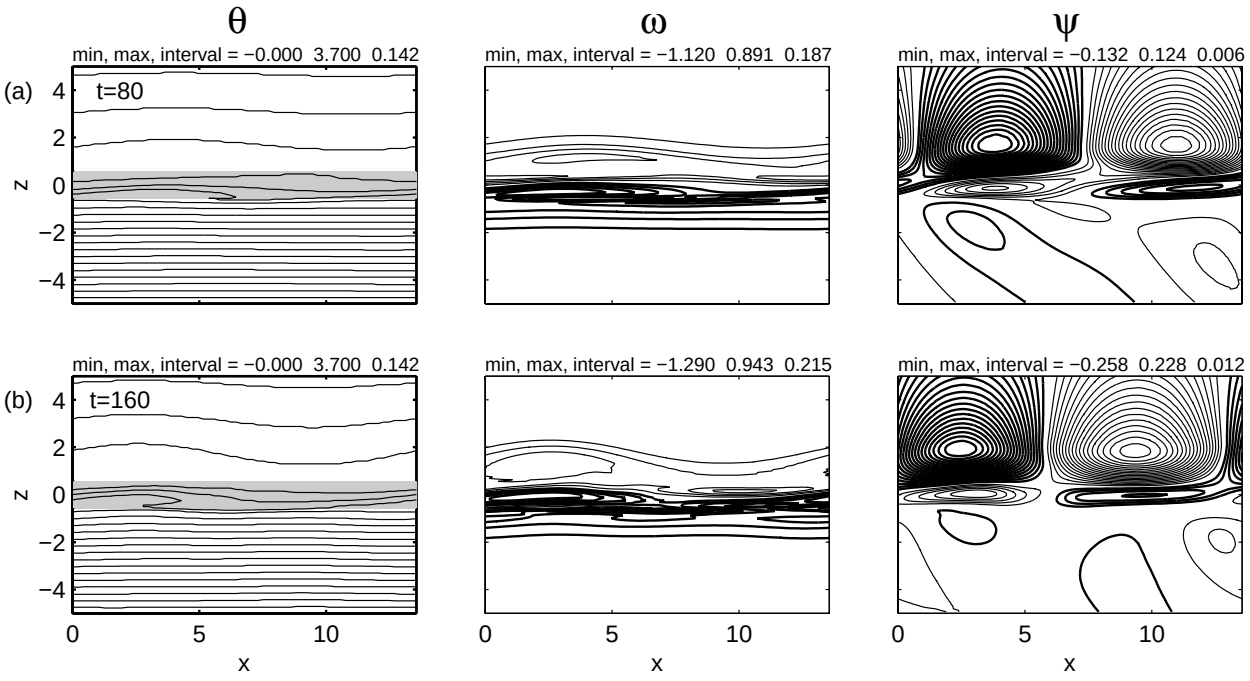

Figure 18: Scaled temperature, vorticity and perturbation streamfunction fields for run R2505 at t=60 (a) and t=120 (b). The perturbation streamfunction is defined relative to the horizontally- averaged profile. Shading indicates the original locations of the critical levels. For the vorticity and the streamfunction, thick (thin) contours indicate negative (positive) values.

With the addition of nonzero stratification in the upper half-space (case R2505), the growth of the R mode is slowed considerably. Not until $t \sim 80$ does significant overturning develop at the lower critical level (figure 18). The secondary instability and subsequent catastrophic breakdown observed in the R25 case is prevented. As in the case R25, wave radiation into the lower half-plane is evident.

The vertical motion of the jet provides a clear indication of wave-mean flow interactions. The location of the velocity centroid ζ as a function of time is shown for all three simulations in figure 19. The S mode at $J_L = 0.14$ displaces the jet upward, as expected on the basis of the momentum flux of the linear eigenmode (cf. figure 7 and accompanying discussion). Displacement of the jet by the R mode with R25 is much slower at first, but increases rapidly after about t=60. This displacement tends to reduce the effect of the stratification. On the basis of our earlier linear stability analyses (e.g. figure 10a), we expect that this will destabilize shorter modes similar to the S mode. (This is confirmed by separate linear stability analyses of the case where the discontinuity in stratification is located below the center of the jet.) This secondary effect of jet migration is the reason for the appearance of the short-wave instability in the R25 case (figure 17) and for the complex evolution of the perturbation kinetic energy (figure 15).

Although the catastrophic breakdown of the jet coincides with the growth of the short-wave secondary instability, the long-wave disturbance is also essential to

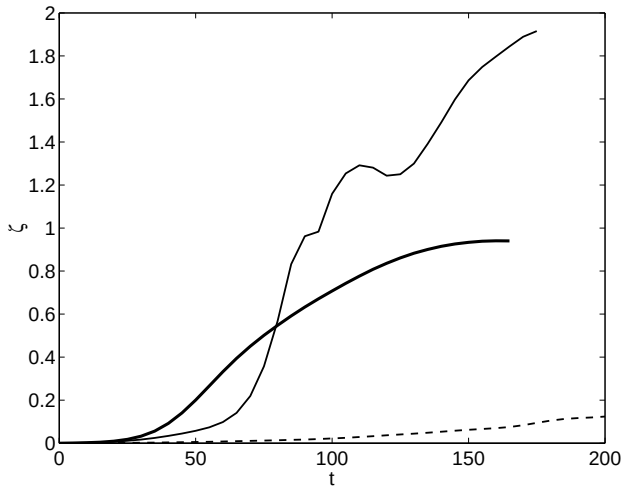

Figure 19: The centroid of the mean velocity distribution as a function of time, showing the vertical migration of the jet center due to the net momentum flux of the unstable mode. Curves correspond to cases S14 (thick solid), S22 (thin solid) and R2505 (dashed).

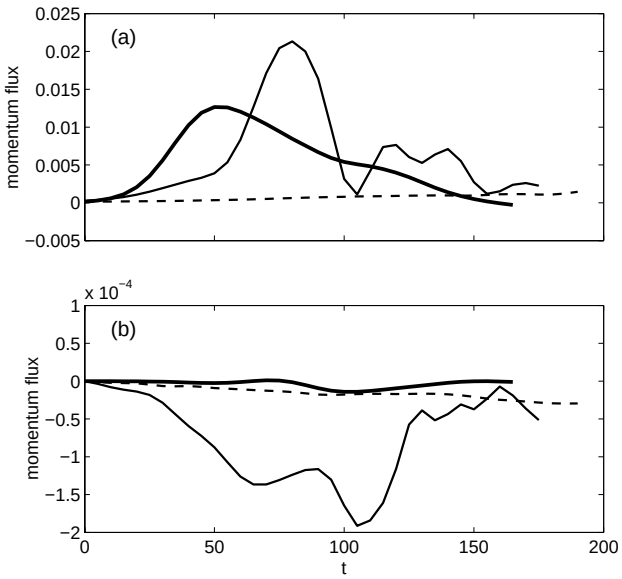

Figure 20: Vertical flux of horizontal velocity across (a) the upper critical level and (b) z=-5. Curves correspond to cases S14 (thick solid), R25 (thin solid) and R2505 (dashed).

the process. A counterexample is provided by simulation S14, which was initialized with the short-wave mode alone. In this case, the disturbance equilibrates at finite amplitude without destroying the jet. In a separate experiment (not shown), the S14 simulation was seeded with a random long-wave disturbance in addition to the short-wave eigenmode. The long-wave component eventually grew to large amplitude and the jet was disrupted as in the R25 case. In run R2505, secondary instability was strongly suppressed by the nonzero stratification in the upper half space.

We conclude this section with a look at the momentum fluxes that arise at two particular levels in our simulations. Fluxes across the upper critical level (figure 20a) correspond to strong instability and overturning above the jet, while fluxes across the lower boundary of the physical domain, $z = -5$ (figure 20b) represent wave propagation into the deep ocean. In the disturbance that develops from the S mode (S14), the momentum flux at the upper critical level grows to a maximum at about the same time that the perturbation kinetic energy peaks (cf. figure 15, $t = 50$). Beyond this point, the disturbance settles into a nonlinear, quasi-equilibrium state in which the momentum flux across the upper critical level drops to zero. This vanishing of the momentum flux is expected, for otherwise the background jet would continue to migrate upwards (rather than remaining steady at $\zeta \sim 1$ as shown in figure 19) and the nonlinear equilibrium state could not be sustained. In case R25, the momentum flux at the upper critical level increases to ~ 0.01 shortly before the secondary instability sets in and the jet begins to migrate (cf. figure 19). The flux then exhibits large amplitude oscillations. When weak stratification is added to the upper half-space (case R2505), the momentum flux at the upper critical level is reduced by more than an order of magnitude. In the R25 and R2505 cases, there is a consistent downward momentum flux at $z = -5$ that grows along with the disturbance

amplitude. In contrast, the momentum flux at z=-5 for the S14 case fluctuates about zero.

5 Comparison with EUC observations

The asymmetrically stratified jet represents an incomplete model of the EUC. It accounts for instability due to the shear on the upper and lower flanks of the jet, and for its modification by the asymmetric stratification profile, but other important factors such as the surface current are omitted from the model. We now compare the characteristics of our computed modes with observational analyses, in order to assess the ability of this limited model to capture the physics of the EUC. We compare our results with the observational results of Moum et al. (1992) and Lien et al. (1996), who observed large-amplitude waves on the upper flank of the EUC, and also with stability analyses of measured profiles from the EUC (Sun et al., 1998).

Appropriate length and velocity scales for the EUC are $h_o = 40m$ and $u_o = 1m/s$ (figure 1). The squared buoyancy above the EUC is rarely greater than $10^{-4}s^{-2}$, whereas typical values just below the EUC vary between 10^{-4} and $10^{-3}s^{-2}$. In our nondimensionalization, these levels of stratification become 0.16 and 1.6, respectively. The domain of interest for the EUC is therefore approximated by $0 \leq J_U \leq 0.16$; $0.16 \leq J_L \leq 1.6$. In the $J_L - J_U$ plane shown on figure 5, this domain occupies a rectangle in the lower right-hand corner that extends to the right beyond the largest value of J_L shown. The R mode dominates over most of this stratification regime. For J_U greater than about 0.1, the flow is stable.

The maximum growth rate of the R mode occurs when J_U vanishes, and is about 0.05. Scaled for the EUC, this gives an e-folding time of about thirteen minutes. This is comparable with the fastest growing modes found by Sun et al. (1998). Typical nondimensional values for the streamwise wavenumber of the R mode are 0.5 (figure 10c) or less. This corresponds to an approximate lower bound on the zonal wavelength of 500m. For comparison, the observations of Moum et al. (1992) and Lien et al. (1996) and the analyses of Sun et al. (1998) all delivered wavelengths in the range 200-350m. In contrast, the wavelength of the S mode is consistent with the observations. Zonal phase speeds of the modes computed by Sun et al. tended to be near zero or even negative, while Lien et al. estimated a phase speed of 0.2m/s. This is in contrast with the phase speed of the R mode, which is generally greater than 0.6, or 0.6m/s in dimensional terms.

The momentum fluxes shown in figure 20a may be compared with the estimates made by Lien et al. (1996) from observations of a large-amplitude wave signal above the core of the EUC. The maximum zonal stress associated with that disturbance was estimated as $0.3Nm^{-2}$. In our nondimensionalization, this becomes $\overline{u'w'} = 3 \times 10^{-4}$. The stresses our model develops above the jet exceed this value by up to two orders of magnitude (figure 20). The most realistic model result is from run R2505, for which the momentum flux at the upper critical level approached 10^{-3} at the end of the simulation. Comparison with the observations of Moum et al. (1992) yields an even wider discrepancy, as their estimates of the momentum flux were an order of magnitude smaller still than those of Lien et al. In addition, accelerations due to the momentum flux convergence in the model are several orders of magnitude stronger than those driven by the zonal pressure gradient in the equatorial Pacific.

It therefore appears that our model develops momentum fluxes that are much more intense than those found on the EUC. The addition of stratification above the jet damps the instabilities considerably, but even the case R2505 develops fluxes that would severely disrupt the EUC over a period of a few hours. This is in dramatic contrast with the EUC, whose large-scale structure varies only on timescales of months to years. These results indicate that instability governed by the main local structure

of the EUC is more than strong enough to account for the observed waves and turbulence; in fact, we must now ask why the EUC is not considerably more turbulent than it is.

6 Summary

We have examined the normal mode instabilities of a Bickley jet in a fluid with asymmetric stratification. We have identified three classes of unstable modes: the S and V modes are extensions of the sinuous and varicose instabilities of the unstratified Bickley jet, while the third mode, denoted "R", has no counterpart in the unstratified case.

Stable stratification in the lower half-space (i.e. $J_L > 0$) damps both the S and V modes. For weak stratification ($J_L < 0.22$), the S mode dominates. At larger J_L, the fastest growing mode is the R mode, whose long wavelength enables it to couple with free IGW modes and thus to radiate energy downward away from the jet. This characteristic is strongly suggestive of the wave radiation observed at depth the in equatorial Pacific.

For $J_L < 0.25$, the R mode appears as a superposition of two oblique disturbances whose wave vectors point at equal and opposite angles from the x axis. The angle of the fastest growing R mode approaches 90 degrees at small J_L, decreases as J_L increases, and vanishes at $J_L = 0.25$. Beyond this point, the dominant R mode is two-dimensional. For $0.22 < J_L < 0.25$, the fastest growing disturbance is a pair of R modes inclined at up to 20 degrees from the x axis. However, these modes grow only marginally faster than their two-dimensional counterparts. Therefore, while three-dimensional primary instability may exert some influence on flow evolution, it is unlikely to be dominant.

The R mode is able to grow despite strong stratification because its energy is focussed on the upper flank of the jet, away from the stratification. Linear theory suggests that, although the R mode resonates with the IGW field in the lower half plane, its lower critical level provides a barrier against energy leakage at sufficiently high J_L. In the nonlinear regime, however, the present simulations reveal no significant change in the downward momentum flux as a function of stratification.

Nonlinear simulations show that both the S and R modes generate strong wave-mean flow interactions at the lower critical layer, leading to overturning of the temperature field that would trigger turbulence in a three-dimensional flow. In both cases, momentum flux divergences cause the jet to migrate upwards away from the stratification. (This migration is reversed in the case of the V mode, but the latter is never dominant.) Migration is slower for the R mode than for the S mode, but when the jet does begin to migrate upward, the result is a dramatic change in the nature of the disturbance. The departure of the jet from the stratified zone destabilizes a short-wave instability similar to the S mode, which grows rapidly and greatly accelerates the breakdown of the jet. It appears that no amount of stratification in the lower half-space alone can prevent this breakdown, though weak stratification in the upper half space stabilizes the jet considerably.

Both linear and nonlinear analyses support the hypothesis that strong turbulence and wave-mean flow interactions on the lower flank of the jet may result from the radiation of gravity waves from the upper flank. Waves are generated by the dynamic instability of the weakly stratified shear on the upper flank, propagate downward, and break upon encountering the critical level on the more strongly stratified lower flank.

With respect to the EUC, the present results lead to an interesting conclusion: if the EUC were simply an isolated jet with stable stratification below and mixed fluid above, it would be torn apart by shear instability within a few hours. In reality, of course, the large-scale structure of the EUC varies only on timescales of months to years. We are thus left with the question: what stabilizes the EUC? A partial answer is provided by the addition

of stratification above the jet, but the momentum fluxes remain at least an order of magnitude larger than observations. In addition, the wavelength of the dominant R mode is longer by a factor of two than that of waves observed near the EUC, and its zonal phase speed is too large. Unrealistically large momentum fluxes can be reduced by increasing J_U to values near the stability boundary, but the discrepancy in wavelength remains.

We now evaluate the potential importance of several factors that are missing from the present model.

- **Three-dimensional motions:** The main effect of three-dimensional turbulence is to smooth gradients via enhanced molecular mixing. In the present two-dimensional simulations, the Reynolds number is set very low (of order 10^2). As a result, the effects of turbulent mixing are at least crudely represented and are, in fact, probably exaggerated.

- **Forcing:** The EUC is sustained by a zonal pressure gradient. In our model, the forcing needed to sustain the jet against instability would have to be several orders of magnitude stronger than that observed in the equatorial oceans. Also, the inclusion of such forcing would increase the momentum fluxes developed in the model, and those fluxes are already too large to match the observations.

- **The seasonal thermocline:** This thin layer of enhanced stratification is located near or slightly below the EUC, and is expected to exert a stabilizing influence.

- **The ocean surface:** Boundary proximity is known to stabilize long modes (e.g. Hazel 1972), and may therefore suppress the R mode that leads to the destruction of the jet in the present simulations. The wavelength of the R mode is much larger than the distance from the jet core to the surface, which means that the boundary proximity effect is likely to be significant.

- **The South Equatorial Current:** The presence of the counterflowing surface current increases the kinetic energy available to drive instability and may thus be expected to destabilize the flow. However, preliminary results indicate that the reverse is true; the surface current actually helps to stabilize the EUC. Also, the presence of the surface current should give rise to modes with small or negative zonal phase velocity, in better agreement with observations.

In summary, it seems likely that better correspondence with observations will result primarily from refinement of the background profiles and the upper boundary condition rather than from the inclusion of forcing or improved turbulence modeling. Future publications will describe extensions of the model to incorporate these factors, leading to improved understanding of waves and instability in the equatorial zonal current system.

Acknowledgements: This work has benefited from discussions with Bruce Sutherland. The research was funded by the National Science Foundation under grant OCE9711872. In the published version of this paper, we neglected to make reference to Skyllingstad and Denbo (1994). That work examined gravity waves and instabilities of the EUC via large-eddy simulations, and was the source of many of the ideas explored here.

References

Dillon, T., J. Moum, T. Chereskin, and D. Caldwell, 1989: Zonal momentum balance at the equator. *J. Phys. Oceanogr.*, **19**, 561–570.

Drazin, P. and W. Reid, 1981: *Hydrodynamic Stability*. Cambridge University Press, Cambridge.

Eliassen, A. and E. Palm, 1961: On the transfer of energy in stationary mountain waves. *Geophys. Publ.*, **22**, 1–23.

Fritts, D., 1989: A review of gravity wave saturation processes, effects, and variability in the middle atmosphere. *Pure Appl. Geophys.*, **130**, 343–371.

Hazel, P., 1972: Numerical studies of the stability of inviscid parallel shear flows. *J. Fluid Mech.*, **51**, 39–62.

Hebert, D., J. Moum, C. Paulson, D. Caldwell, T. Chereskin, and M. McPhaden, 1991: The role of the turbulent stress divergence in the equatorial pacific zonal momentum balance. *J. Geophys. Res.*, **96**, 7127–7136.

Klaassen, G. and W. Peltier, 1985b: The onset of turbulence in finite-amplitude Kelvin-Helmholtz billows. *J. Fluid Mech.*, **155**, 1–35.

Lien, R.-C., D. Caldwell, M. Gregg, and J. Moum, 1995: Turbulence variability at the equator in the central pacific at the beginning of the 1991-1993 El Nino. *J. Geophys. Res.*, **100**(C4), 6881–6898.

Lien, R.-C., M. McPhaden, and M. Gregg, 1996: High-frequency internal waves and their possible relationship to deep-cycle turbulence. *J. Phys. Oceanogr.*, **26**, 581–600.

Lin, C.-L., J. Ferziger, J. Koseff, and S. Monismith, 1993: Simulation and stability of two-dimensional internal gravity waves in a stratified shear flow. *Dyn. Atmos. Oceans*, **19**, 325–366.

Lindzen, R., 1981: Turbulence and stress due to gravity wave and tidal breakdown. *J. Geophys. Res.*, **86**, 9707.

Lindzen, R. and K. Tung, 1978: Wave overreflection and shear instability. *J. Atmos. Sci.*, **35**, 1626–1632.

Mack, A. and D. Hebert, 1997: Internal gravity waves in the upper eastern equatorial Pacific: Observations and numerical solutions. *J. Geophys. Res.*, **102**, 21081–21100.

Moum, J., D. Caldwell, and C. Paulson, 1989: Mixing in the equatorial surface layer and thermocline. *J. Geophys. Res.*, **94**(C2), 2005–2021.

Moum, J., D. Hebert, C. Paulson, and D. Caldwell, 1992: Turbulence and internal waves at the equator. Part I: Statistics from towed thermistor chains and a microstructure profiler. *J. Phys. Oceanogr.*, **22**, 1330–1345.

Peters, H., M. Gregg, and J. Toole, 1989: Meridional variability of turbulence through the equatorial undercurrent. *J. Geophys. Res.*, **94**, 18003–18009.

Qiao, L. and R. Weisberg, 1997: The zonal momentum balance of the equatorial undercurrent in the Central Pacific. *J. Phys. Oceanogr.*, **27**, 1094–1119.

Skyllingstad, E. and D. Denbo, 1994: The role of internal gravity waves in the equatorial current system. *J. Phys. Oceanogr.*, **24**, 2903–2110.

Smyth, W., G. Klaassen, and W. R. Peltier, 1988: Finite amplitude Holmboe waves. *Geophys. Astrophys. Fluid Dyn.*, **43**, 181–222.

Smyth, W. and W. Peltier, 1989: The transition between Kelvin-Helmholtz and Holmboe instability: an investigation of the overreflection hypothesis. *J. Atmos. Sci.*, **46**(24), 3698–3720.

Smyth, W. and W. Peltier, 1990: Three-dimensional primary instabilities of a stratified, dissipative, parallel flow. *Geophys. Astrophys. Fluid Dyn.*, **52**, 249–261.

Sun, C., W. Smyth, and J. Moum, 1998: Dynamic instability of stratified shear flow in the upper equatorial Pacific. *J. Geophys. Res.*, **103**, 10323–10337.

Sutherland, B., 1996: Dynamic excitation of internal gravity waves in the equatorial oceans. *J. Phys. Oceanogr.*, **26**, 2398–2419.

Sutherland, B., C. Caulfield, and W. Peltier, 1994: Internal gravity wave radiation and hydrodynamic instability. *J. Atmos. Sci.*, **51**, 3261–3280.

Sutherland, B. and W. Peltier, 1992: The stability of stratified jets. *Geophys. Astrophys. Fluid Dyn.*, **66**, 101–131.

Veronis, G., 1960: An approximate theoretical analysis of the equatorial undercurrent. *Deep Sea Res.*, **6**, 318–327.

Winters, K. and E. A. D'Asaro, 1993: Two-dimensional instability of finite amplitude internal gravity waves near a critical level. *J. Geophys. Res.*, **94**, 12709–12719.

Winters, K. and E. A. D'Asaro, 1994: Three-dimensional wave instability near a critical layer. *J. Fluid Mech.*, **272**, 255–284.